PARTICLE SPECTROMETERS

This article introduces the reader to the field of high-energy physics and the subatomic-particle detection techniques that it employs. These techniques are of interest to the electrical engineer because they often entail sophisticated signal-processing and data-acquisition systems. We begin with an overview of the field, and then briefly introduce subatomic particles and their detection before treating particle detectors in more detail. We conclude with two examples that illustrate how a variety of detectors work together in typical high-energy-physics experiments.

The experimental study of subatomic particles and their interactions has revealed an unexpected layer of substructure underlying the atomic nucleus and has shed light on the evolution of the universe in the earliest moments following the Big Bang. This field of research is commonly referred to as elementary-particle physics or (because of the highly energetic particle beams employed) high-energy physics.

Modern subatomic-particle experiments employ elaborate spectrometry systems, often with state-of-the-art electronic instrumentation. While there is much variation among spectrometers, generally they measure the trajectories and energies of subatomic particles passing through them. In a typical experiment, a beam of subatomic particles is brought into collision with another particle beam or with a stationary target. Interactions between particles yield reaction products, some of which pass through the spectrometer. Measurements can include the momentum, angle, energy, mass, velocity, and decay distance of reaction products.

Particle-detection techniques pioneered in high-energy physics have received broad application outside that field. Im-

J. Webster (ed.), *Wiley Encyclopedia of Electrical and Electronics Engineering*.

portant examples include nuclear physics, astronomy, medical imaging, X-ray scattering, diffraction, and spectroscopy, and the use of synchrotron radiation in biophysics, biochemistry, materials science, and the semiconductor industry (1,2). There has of course been intellectual traffic in both directions, for example, the pioneering use of semiconductor detectors in nuclear physics and of charge-coupled devices (CCDs) in astronomy (3).

OVERVIEW OF SUBATOMIC PARTICLES

Subatomic particles include the familiar electron, proton, and neutron, which are the components of the atom. In addition, dozens of less stable particles have been discovered since the 1930s that can be produced in reactions among electrons, protons, and neutrons and subsequently decay in a variety of ways. Each particle is characterized by a unique set of values for mass, electric charge, average lifetime, etc. Subatomic particles also possess a property called spin, which differs from the classical concept of angular momentum in that it is quantized (in units of $\hbar/2$) and immutable. Table 1 defines the units of measurement commonly used in high-energy physics for these quantities that are employed in this article.

Leptons, Hadrons, and Gauge Bosons

Since the 1960s a simple unifying principle for the plethora of subatomic particles has become generally accepted. Subatomic particles fall into three categories: leptons, hadrons, and gauge bosons [see Table 2 (4)]. The hadrons are made of quarks (described later). Leptons and quarks each have one quantum of spin, while gauge bosons have two or four spin quanta. Gauge bosons are responsible for the forces between particles. For example, the electromagnetic force arises from the exchange of photons among charged particles, and the strong force from the exchange of gluons.

Leptons and hadrons can be distinquished experimentally by their modes of interaction. Hadrons are subject to the strong force (which also binds the nucleus together), while leptons are not. There are only six types of lepton: the (negatively charged) electron, muon, and tau and their neutral partners, the electron neutrino, muon neutrino, and tau neutrino. The three charged leptons all have charge $-1e$. For each type of lepton there exists a corresponding antiparticle. Lepton and antilepton have equal mass, spin, and lifetime, and electric charges equal in magnitude but (for charged leptons) opposite in sign.

Quarks

The hadrons are composed of quarks, of which (like the leptons) only six types are known. These are designated up and down, charm and strange, and top and bottom [see Table 3 (4)]. (For historical reasons, the top and bottom quarks are also designated by the alternative names truth and beauty; somewhat illogically, top and beauty are the names more commonly used.) Like the leptons, the quarks come in pairs with the members of a pair differing in electric charge by one unit. The up, charm, and top quarks have charge $+\frac{2}{3}e$. The down, strange, and bottom quarks have charge $-\frac{1}{3}e$. For each type of quark there exists a corresponding antiquark with opposite electric charge.

Quarks are bound together into hadrons by the strong force. This is observed to occur in two ways: a quark can bind to an antiquark to form a meson or antimeson, and three quarks or antiquarks can bind together to form a baryon or antibaryon. Bare quarks, as well as combinations of quarks other than those just mentioned, have never been observed and are presumed to be forbidden by the laws governing the strong force. (The possible existence of hadrons made up entirely of gluons is a subject of current experimental investigation but has not been definitively established.)

OVERVIEW OF PARTICLE DETECTION

Subatomic particles can be detected via their interactions with bulk matter. Most particles can interact via more than one of the four forces (in order of decreasing interaction strength): strong, electromagnetic, weak, and gravitational. It is typically the stronger forces that give the most dramatic and easily detectable signals. Since subatomic particles have such small masses, the gravitational force is entirely useless for their detection. All charged particles can be detected via the electromagnetic force, since they ionize nearby atoms as they pass through matter. Neutrinos (which as neutral leptons "feel" only the weak and gravitational forces) are exceedingly difficult to detect directly, and their production is typically inferred via conservation of momentum and energy by observing that some of the momentum and energy present before a reaction are missing in the final state.

Position Measurement: Hodoscopes and Telescopes

Detectors that measure particle position can be arranged as *hodoscopes* or *telescopes*. Hodoscopes are arrays of adjacent detectors typically used to measure the position of a particle along a direction perpendicular to the particle's path. Tele-

Table 1. Units Commonly Used in High-Energy Physics

Quantity	Unit	Value in MKS units[a]	Comment
Charge	e	1.60×10^{-19} C	
Energy	electron volt (eV)	1.60×10^{-19} J	Kinetic energy of particle of charge e accelerated through 1 V.
Mass	GeV/c^2[b]	1.78×10^{-27} kg	Mass and energy related by $E = mc^2$.
Momentum	GeV/c[b]	5.34×10^{-19} kg · m/s	
Spin	$\hbar$	1.05×10^{-34} J · s	Reduced Planck constant; spin quantum is $\hbar/2$.

[a] Values are quoted to three significant digits, which is sufficient precision for most purposes.
[b] 1 GeV = 10^9 eV.

Table 2. Properties of Selected Subatomic Particles[a,b]

Particle	Symbol	Charge (e)	Mass (GeV/c^2)	Mean Life (s)	Spin ($\hbar$)	
			Leptons			
Electron	e^-	−1	5.11×10^{-4}	Stable	$\frac{1}{2}$	
Electron neutrino	ν_e	0	0	Stable	$\frac{1}{2}$	
Muon	μ^-	−1	0.105	2.20×10^{-6}	$\frac{1}{2}$	
Muon neutrino	ν_μ	0	0	Stable	$\frac{1}{2}$	
Tau	τ^-	−1	1.78	2.91×10^{-13}	$\frac{1}{2}$	
Tau neutrino[c]	ν_τ	0	0	Stable	$\frac{1}{2}$	
			Hadrons			Quark content
			Baryons			
Proton	p	+1	0.938	stable	$\frac{1}{2}$	uud
Neutron	n	0	0.940	887	$\frac{1}{2}$	udd
Lambda	Λ	0	1.12	2.63×10^{-10}	$\frac{1}{2}$	uds
Cascade	Ξ^-	−1	1.32	1.64×10^{-10}	$\frac{1}{2}$	dss
	Ξ^0	0	1.31	2.90×10^{-10}	$\frac{1}{2}$	uss
			Mesons			
Pion	π^+, π^-	+1, −1	0.140	2.60×10^{-8}	0	$u\bar{d}$, $d\bar{u}$
	π^0	0	0.135	8.4×10^{-17}	0	$u\bar{u}$, $d\bar{d}$
Kaon	K^+, K^-	+1, −1	0.494	1.24×10^{-8}	0	$u\bar{s}$, $\bar{u}s$
	K^0, $\bar{K}^0$	0	0.498	[d]	0	$d\bar{s}$, $s\bar{d}$
J/psi	J/ψ	0	3.10	1.25×10^{-19}	1	$c\bar{c}$
B	B^+, B^-	+1, −1	5.28	1.62×10^{-12}	0	$u\bar{b}$, $b\bar{u}$
	B^0, $\bar{B}^0$	0	5.28	1.56×10^{-12}	0	$d\bar{b}$, $b\bar{d}$
			Gauge bosons			Force mediated
Photon	γ	0	0	Stable	1	Electromagnetic
Weak bosons	W^+, W^-	+1, −1	80.3	1.59×10^{-25}	1	Weak
	Z^0	0	91.2	1.32×10^{-25}	1	Weak
Gluons	g	0	0	Stable	1	Strong
Graviton[c]	G	0	0	Stable	2	Gravitational

[a] Data presented here are for illustrative purposes; more complete and detailed information is available in the *Review of Particle Physics* (4), published biennially and available on the World-Wide Web at http://pdg.lbl.gov.
[b] Values are quoted to three significant digits, which is sufficient precision for most purposes.
[c] The existence of these particles has been postulated but is not yet definitively established.
[d] Due to mixing of neutral kaons with their antiparticles, these particles do not have definite lifetimes. Symmetric and antisymmetric linear combinations of K^0 and $\bar{K}^0$, known as K_S and K_L, have lifetimes of 8.93×10^{-11} s and 5.17×10^{-8} s, respectively.

scopes are arrays of detectors arranged sequentially along the particle's path so as to track the motion of the particle.

Commonly used position-sensitive detectors include scintillation counters, solid-state detectors, proportional tubes, and multiwire proportional and drift chambers. These produce electrical signals that can be digitized and processed in real time or recorded for further analysis using high-speed digital computers. Specialized detectors less commonly used nowadays include the cloud chamber and bubble chamber, in which measurements are made continually as the particle traverses an extended gaseous or liquid medium, the spark chamber, and stacks of photographic emulsion. These detectors typically produce information on photographic film that must be processed optically, requiring scanning and measurement by trained personnel.

Table 3. The Three Generations of Quarks and Antiquarks[a]

Charge (e)	Spin ($\hbar$)	Generation 1		Generation 2		Generation 3	
				Quarks			
+2/3	1/2		u		c		t
−1/3	1/2	d		s		b	
				Antiquarks			
+1/3	1/2	$\bar{d}$		$\bar{s}$		$\bar{b}$	
−2/3	1/2		$\bar{u}$		$\bar{c}$		$\bar{t}$
Approx. mass (GeV/c^2):		0.01	0.005	0.25	1.3	4.2	180

[a] After "Review of Particle Physics" (4).

Momentum and Energy Measurement

Magnetic Spectrometry. In a magnetic field, charged particles follow helical trajectories. The radius of curvature is proportional to the particle momentum and inversely proportional to the particle charge and the field strength. Given the radius r in meters, momentum p in GeV/c, charge q in units of the electron charge, and field strength B in tesla,

$$r = 0.3 \frac{p}{qB \sin\theta} \tag{1}$$

where θ is the angle between the field direction and the particle momentum vector. From measurements of the curvature

of the particle track within the field, the momentum can thus be determined. Even if no measurements are made within the field, the curvature within it (and hence the momentum) can be inferred by measuring the particle's trajectory before and after it traverses the field. The magnetic field, typically in the range 1 T to 2 T, is generally produced using an electromagnet, which may be air core or solid and have conventional (copper or aluminum) or superconducting coils.

Calorimeters. Calorimeters are detectors of thickness sufficient to absorb as large a fraction as possible of the kinetic energy of an incident particle. While for electrons and hadrons this fraction can approach 100 %, there is usually some leakage of energy out the back of a calorimeter. An electrical signal is produced proportional to the deposited energy. Unlike tracking detectors, calorimeters can detect neutral as well as charged particles. Calorimeters also play an important role in electron identification and are sometimes used for muon identification, as described next.

Particle Identification

Of the charged subatomic particles, five are sufficiently stable to travel many meters at the energies typical in high-energy physics (1 GeV to several hundred GeV), so that their trajectories can be easily measured in a magnetic spectrometer. The problem of particle identification is thus that of distinguishing among these five particles: electrons, muons, pions, kaons, and protons. In experiments that identify particles, multiple particle-identification techniques are typically used together in order to enhance the efficiency of identification and lower the probability of misidentification.

Calorimetric Electron (and Photon) Identification. As discussed in more detail in later sections, in material of high atomic number (Z), high-energy electrons create characteristic electromagnetic showers consisting of a cascade of photons, electrons, and antielectrons (positrons). Thus the pattern of energy deposition in a calorimeter, as well as the correlation of deposited energy with magnetically measured momentum, can be used to distinguish electrons from other charged particles. In a calorimeter optimized for this purpose, e–π rejection of 10^{-4} can be achieved (i.e., only 10^{-4} of pions mistaken for electrons) (5), while maintaining 75% efficiency for electrons (i.e., only 25% of electrons rejected as having ambiguous identification) (6).

Since high-energy photons also create electromagnetic showers in high-Z materials, electromagnetic calorimetry can also be used to identify photons and measure their energy. Photons are distinguishable from electrons since they do not give observable tracks in tracking telescopes.

Muon Identification. Muons (and also neutrinos) are distinguished from other charged particles by their low probability to interact with nuclei: muons can pass through many meters of iron while depositing only ionization energy. A muon can thus be identified efficiently and with little background, with typical μ–π rejection of order 10^{-2} (7), by its failure to shower in a calorimeter. Often for muon identification, instead of a full calorimeter, a crude structure is used consisting of thick shielding layers of steel or concrete interspersed with detectors; an example of such a muon-identification system is shown in Fig. 6.

Time of Flight and Ionization. If a particle's momentum is known from magnetic spectroscopy, measurement of its velocity determines its mass. At momenta up to a few GeV/c, particle velocity can be measured well enough for particle identification using time-of-flight measurement over a distance of order meters (8). This is typically accomplished using thick (several centimeters) scintillation counters (discussed later) to determine flight time to a fraction of a nanosecond. This information is often augmented by repeated measurements of ionization rate in proportional chambers since (as described later) the rate of ionization in a medium is velocity dependent.

Cherenkov Detectors. Particle velocity can be measured (or limits can be placed on it) using the Cherenkov effect, by which a charged particle moving through a transparent medium at a speed greater than the speed of light in that medium emits photons at a characteristic velocity-dependent angle. (This process is mathematically analogous to the emission of sonic boom by a supersonic object or the creation of a bow wave by a fast-moving boat.) The speed of light in a medium is slower than the speed of light in vacuum by the factor $1/n$, where n is the medium's refractive index.

Threshold Cherenkov counters (9) determine limits on a particle's speed by establishing that the particle does or does not emit Cherenkov photons in media of various refractive indices. Several threshold Cherenkov counters with appropriately chosen thresholds can be used together to distinguish pions, kaons, and protons within a given momentum range. This technique is typically useful from about 1 GeV/c up to several tens of GeV/c. Ring-imaging Cherenkov counters (10) measure the particle's speed by determining the photon-emission angle directly, and can be used up to a few hundred GeV/c.

Note that Cherenkov detectors are rarely useful for muon identification, since muons and pions are so similar in mass that their Cherenkov thresholds (and photon-emission angles) are nearly indistinguishable in practice.

Transition-Radiation Detectors. Transition radiation consists of photons emitted when a charged particle crosses an interface between media of differing refractive index. Particles with "highly relativistic" velocity (i.e., with kinetic energy greatly exceeding their mass energy) produce detectable numbers of "soft" X rays (energy of order a few kiloelectronvolts) when traversing stacks of thin metal or plastic foils typically including hundreds of interfaces. These X rays can be detected in proportional chambers and used for e–π discrimination at momenta exceeding 1 GeV/c and hadron (π, K, or p) identification up to a few hundred GeV/c (11). Using calorimetry and transition-radiation detection together, e–π rejection of 10^{-5} has been achieved (12).

PROBABILISTIC NATURE OF PARTICLE REACTIONS

Since subatomic-particle spectrometers deal with the smallest objects we know of, they encounter directly the statistical aspects of quantum mechanics and the "microworld." It is a striking feature of the laws of quantum mechanics that they do not predict the outcome of individual particle reactions but only particle behavior on the average. Nevertheless, most aspects of particle detection can be understood using classical

physics, and quantum uncertainty is rarely a dominant contribution to measurement error.

Example 1: Elastic Scattering

As a first example, if we consider a proton colliding elastically with another proton, classical physics predicts exactly the scattering angle as a function of the impact parameter (the distance between the centers of the protons measured perpendicular to the line of flight). However, quantum mechanically the proton is described not as a hard sphere with a well-defined radius, but rather as a wave packet, with the square of the wave's amplitude at any point in space giving the probability for the proton to be at that location. The impact parameter in any given collision is thus an ill-defined quantity. It is not necessary to delve into the mathematical complexities of quantum mechanics to realize that in this situation the scattering angle for a given encounter is a random and unpredictable quantity. What the laws of quantum mechanics in fact predict is the *probability* for a proton to scatter through any given angle, in other words, the scattering-angle *distribution*. The random nature of quantum mechanics underlies Heisenberg's famous uncertainty relations, which give the fundamental limits to the accuracy with which any quantity can be measured.

Example 2: Inelastic Scattering

Next we consider an *inelastic* collision between two protons, in which one or both protons emerge in excited states that decay into multiple-particle final states. This is a common type of interaction event of interest in high-energy physics, since from the properties and probability distributions of the final state can be inferred various properties of the protons, their constituent quarks and gluons, and the interactions among them. In any given encounter between two protons, whether an inelastic collision will take place cannot in principle be predicted, nor, if so, what particles will be produced and with what momentum and spin vectors. What quantum mechanics *does* predict (in principle) is the *distributions* of these quantities over a large number of collisions. However, since we do not yet have a completely satisfactory theory of the strong force, these distributions cannot as yet be predicted in detail from "first principles."

Classical Uncertainty

One should note that uncertainty in the outcome or measurement of an event is often not quantum mechanical in origin. For example, even classically, the angle of elastic scattering of a given proton incident on a target is in practice not predictable, since it is not feasible to measure the position of the proton with respect to the scattering nucleus with sufficient precision to know the impact parameter. Thus even a classical analysis of the problem predicts only the scattering-angle distribution.

Measurement Resolution

When measurement yields a distribution for some parameter rather than a definite value, we can characterize the quality of the measurement by the width of the distribution, that is, the measurement *resolution* or uncertainty. Common ways of characterizing the width of a distribution are the root-mean-square (rms) deviation and the full width at half maximum (FWHM). Of course, if looked at in fine enough detail, any measurement yields a distribution, though the distribution may be extremely narrow in some cases.

A broad distribution in the result of some measurement can reflect quantum-mechanical uncertainty or simply lack of knowledge of the exact input state. Later we consider examples of both classical and quantum contributions to measurement resolution.

Randomness and Experimental Instrumentation

For the designer of particle-spectrometry systems, a consequence of these uncertainties is that randomness must be taken into account. For example, one might be designing data-acquisition equipment for an experiment intended to operate at an event rate of 100 kHz. This means that on average one has 10 μs to acquire and process the information from each event, but the actual number of events occurring in a given time interval will be random and characterized by a Poisson probability distribution [see Eq. (3)]. Thus if a large fraction of all events are to be captured, data acquisition for each event must be accomplished in a time that is short compared to 10 μs (in this example), to keep sufficiently small the probability that a second event occurs while the first is being processed.

DETAILED DISCUSSION OF PARTICLE DETECTORS

All detectors of subatomic particles operate by virtue of the energy lost by charged particles as they traverse matter. Charged particles lose energy in matter by several mechanisms. These include ionization of nearby atoms, bremsstrahlung (emission of photons in the electric field of an atomic nucleus), Cherenkov and transition radiation, and strong nuclear interactions. For all charged particles except electrons, ionization typically dominates over other mechanisms. The key challenge to particle detection is amplification of the small signals (typically tens to thousands of photons or electrons) produced by these mechanisms.

Ionization Energy Loss

The rate dE/dx of ionization energy loss by a charged particle passing through material depends primarily on the particle's speed, or more precisely on the quantity

$$\beta\gamma = \frac{v/c}{\sqrt{1-(v/c)^2}} \tag{2}$$

where $\beta \equiv v/c$ is the particle's speed expressed as a fraction of the speed of light in vacuum, and the *time dilation factor* $\gamma = 1/\sqrt{1-(v/c)^2}$. (Note that $\beta\gamma$ reduces to v/c in the nonrelativistic limit $v \ll c$.) The rate of ionization is given by the Bethe–Bloch equation; see Ref. 4 for details. As shown in Fig. 1 (4), slow particles are heavily ionizing. The rate of ionization energy loss drops with increasing $\beta\gamma$ approximately as $(\beta\gamma)^{-5/3}$ to a minimum at a value of $\beta\gamma$ that depends only slightly on the material. The ionization minimum is at $\beta\gamma = 3.5$ for nitrogen, which decreases to $\beta\gamma = 3.0$ for high-Z materials such as lead.

While dE/dx per unit thickness varies substantially among materials, if the thickness is divided by density, thus being expressed as mass per unit area, the strongest part of

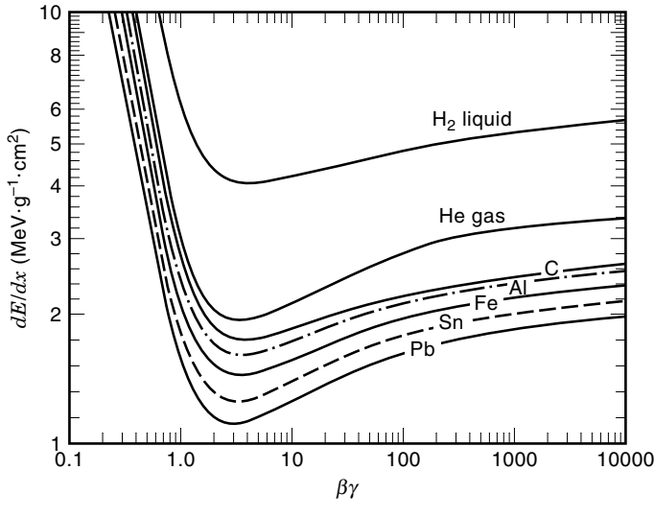

Figure 1. The dependence of the ionization energy-loss rate on the relativistic speed variable $\beta\gamma$ for particles of charge e (except electrons) in various materials (after Fig. 22.2 of Ref. 4). The ionization rate first drops approximately as $\beta\gamma^{-5/3}$, then rises logarithmically. Particles with $\beta\gamma > 1$ (speed greater than $c/\sqrt{2}$) can loosely be considered *minimum-ionizing*.

the dependence on material is eliminated. For particles of charge e (except electrons), and for all materials except hydrogen, the energy-loss rates at the ionization minimum range from 1 MeV/(g/cm^2) to 2 MeV/(g/cm^2). For $\beta\gamma$ above minimum-ionizing, the ionization energy-loss rate rises approximately logarithmically. At $\beta\gamma = 10^4$, the loss rate is less than double relative to its minimum at $\beta\gamma \approx 3$. In this ultrarelativistic regime radiative energy loss (bremsstrahlung) becomes significant relative to ionization.

Radiation Length

In materials of high atomic number, there is a high probability per unit length for electromagnetic radiative processes to occur, that is, for electrons to radiate photons by bremsstrahlung and for photons to convert into electron–positron pairs in the electric field of a nucleus. This probability is characterized by the *radiation length* X_0 of the material, defined as the thickness of material in which a high-energy electron will lose all but a fraction $1/e$ of its initial energy (13). Radiation length also characterizes the degree to which charged particles scatter randomly, due to multiple encounters with the electric fields of nuclei, in passing through material. If precise measurement of particle trajectories is to be achieved, this scattering effect must be minimized. Materials with short radiation length (e.g., lead, $X_0 = 0.56$ cm, and tungsten, $X_0 = 0.35$ cm) are thus desirable for use in electromagnetic sampling calorimeters (discussed later) and in some shielding applications, but in general should be avoided in other particle-detection contexts.

Scintillation Counters

Scintillators (14) are materials in which some of the ionization energy lost by a charged particle along its trajectory is converted into light via fluorescence. The light may be detected in a variety of ways, including (most commonly) photomultiplier tubes and solid-state photodetectors. Both organic and inorganic scintillators are in use.

Organic Scintillators. Organic scintillators typically consist of aromatic liquids dissolved in a plastic such as polystyrene, polyvinyltoluene, or polymethylmethacrylate. Liquid scintillators, more common in the past, have generally been abandoned in high-energy physics (except in specialized applications) in favor of the plastic scintillators, which offer greater ease of use. A common configuration is a piece of plastic of a few millimeters to a few centimeters thickness, a few to several centimeters width, and length ranging from several centimeters to a few meters, glued at one end to a plastic *light guide* that is in turn glued to or butted against the entrance window of a photomultiplier tube (PMT).

A minimum-ionizing charged particle traversing the plastic deposits ionization energy at a rate of about 2 MeV/(g/cm^2). As the ionized plastic molecules deexcite, they emit ultraviolet photons, most of which are quickly reabsorbed by the plastic. To provide a detectable light signal, the plastic is doped with a low concentration of dissolved aromatic "wavelength shifters" (fluors) such as *p*-terphenyl, 3-hydroxyflavone, and tetraphenylbutadiene. These absorb in the ultraviolet and reemit at visible wavelengths, where the plastic is transparent. (Since there is inevitably some overlap between the wavelength-shifter absorption and emission bands, too large a concentration of wavelength shifter would result in excessive attenuation of the light signal as it travels towards the photodetector.)

In a counter of large length-to-width ratio, light collection is inherently inefficient, since only a narrow range of emission angle is subtended by the photodetector. Furthermore, the light is attenuated by absorption along the length of the counter. Light is typically emitted at a rate of about 1 photon per 100 eV of ionization energy, but often only a few percent of these reach the photodetector, where additional losses may be incurred due to reflection at the interfaces. The quantum efficiency of the photodetector further reduces the signal. For a PMT, the quantum efficiency is the probability that an incident photon causes the emission of an electron from the photocathode. The typical PMT visible-light quantum efficiency is about 20%, but solid-state photodetectors can have quantum efficiencies approaching 100% (15). Since photodetectors are subject to single-electron shot noise, the typical signal-to-noise ratio in a plastic scintillation counter of about 1 cm thickness is of order 10 to 100.

With fast fluors, the light signal develops quite rapidly (rise times of order nanoseconds). Instantaneous counting rates of the order of 10 MHz can be sustained. With high-speed PMTs, thick scintillators can achieve subnanosecond timing accuracy, ideal for time-of-flight particle identification. Average counting rates are limited by the current ratings of the PMT and base. In high-counting-rate applications, transistorized bases (16) are crucial to avoid "sagging" of the dynode voltages.

Scintillating Fibers. In recent years advances in photodetectors and in the manufacture of plastic optical fibers have made scintillating optical fibers a practical detector for precision particle tracking at high rates (17). Scintillating fibers work by trapping scintillation light through total internal reflection. Since the fibers are typically less than 1 mm in diameter, detection of the scintillation signal is technically chal-

lenging: the ionization signal is only of the order of 10^3 photons, and the light trapping efficiency of the order of 1%. To convert the scintillation photons efficiently to visible light, wavelength shifters of large *Stokes shift* (i.e., large separation between the absorption and emission bands) are required so that they can be used in sufficiently high concentration (of order 1%) without excessive attenuation. If the light is detected with solid-state cryogenic visible-light photon counters (VLPCs) (18), advantage can be taken of their 80% quantum efficiency, so that a trapped-photon yield as low as several per minimum-ionizing particle suffices for good detection efficiency [see Eq. (3)]. Fibers as narrow as 800 μm in diameter can then be used over lengths of meters (19). An advantage of the large Stokes shift is operation in the green region of the visible spectrum (as opposed to the blue of conventional scintillators), so that yellowing of the plastic due to radiation damage in the course of a high-rate experiment has only a slight impact on performance.

Inorganic Scintillators. Inorganic scintillators include doped and undoped transparent crystals such as thallium-doped sodium iodide, bismuth germanate, cesium iodide, and lead tungstate. They feature excellent energy resolution and are typically employed in electromagnetic calorimetry (discussed later). Some notable recent applications (20) have featured silicon-photodiode readout, allowing installation in the cramped interior of colliding-beam spectrometers as well as operation in high magnetic fields.

Proportional and Drift Chambers

Developed starting in the 1960s by Charpak et al. (21), proportional and drift chambers have largely supplanted visualizing detectors, such as bubble chambers, as the workhorse detectors of high-energy physics due to their higher rate capability and their feasibility of manufacture and operation in large sizes. They typically can provide submillimeter spatial resolution of charged-particle trajectories over volumes of several m^3 (22). Installations of these detectors are commonly realized as hodoscopic arrays of anode wires immersed in a suitable gas mixture and arranged so as to detect the ionization energy released when the gas is traversed by a charged particle. The passage of the particle causes an electrical pulse on the nearest wire, yielding, with the simplest type of signal processing, discrete coordinate measurements (i.e., the true position of the particle is approximated by the location of the wire). Continuous coordinate measurements can be achieved by more sophisiticated signal processing that provides interpolation between anode wires. Although the primary use of these detectors is for position measurement, they also find use in particle identification in the detection of transition radiation and the measurement of ionization rate (dE/dx).

Proportional-Tube Operating Principle. Many proportional-chamber arrangements have been devised. The simplest conceptually is the proportional tube, in which a single thin anode wire is operated at a positive potential (of order kilovolts) with respect to a surrounding conducting cathode surface. The tube is filled with a gas suitable for detecting the particles of interest. For example, charged particles are readily detected in a variety of mixtures of argon with hydrocarbons, while detection of X rays, for example, from transition radiation or crystal scattering, is more efficiently accomplished using a higher-Z gas (such as xenon) as the major component. The exact choice of gas mixture also depends on such experimental requirements as rate capability, position resolution, and detector operable life-span (23).

Size of Primary Ionization Signal. A minimum-ionizing charged particle traversing a proportional tube deposits only a small fraction of its energy in the gas, in a number of ionizing collisions averaging about 0.5 to 5 per mm · atm, depending on gas composition. Due to the independent and random nature of the collisions, they are characterized by Poisson statistics, that is,

$$P(n) = \frac{\mu^n e^{-\mu}}{n!} \tag{3}$$

where $P(n)$ is the probability to produce n ionizing collisions when the mean number produced is μ. Furthermore, because of the wide range of energies imparted in these collisions, the yield of electron-ion pairs is subject to large fluctuations (24). Consequently, amplification electronics designed to detect the passage of minimum-ionizing particles through the tube should be capable of handling the large dynamic range (typically exceeding 10) of these signals. In contrast, soft X rays interact in the gas primarily via the photoelectric effect, giving a narrower range of signal sizes since the amount of ionization is more closely correlated with the X-ray energy.

Electron and Ion Drift. Under the influence of the electric field in the tube, the electrons and positive ions produced by the initial interaction separate and drift toward the anode and cathode, respectively. In the range of electric-field strength E typically found in proportional tubes, the average drift velocity u^+ of the positive ions is proportional to E; it is often expressed in terms of the ion mobility $\mu^+ = u^+/E$. This proportionality results from competition between two effects: acceleration of the ion by the electric field and randomization of its direction by collisions with gas molecules. A typical drift field E = 1 kV/cm gives an ion drift velocity in the range (0.5 to 2) $\times$ 10^3 cm/s depending on ion species and gas composition.

In weak electric fields, electrons are transported in a manner similar to that of positive ions. However, in a sufficiently strong electric field, the electron's wavelength λ, which decreases in inverse proportion to its momentum p according to the deBroglie relationship $\lambda = h/p$, becomes comparable to the size of molecular orbitals. (Here h is Planck's constant.) In this regime, the probability per encounter for an electron to scatter off of a molecule has a strong dependence on the electron momentum, displaying successive minima and maxima as the momentum increases. In many gas mixtures, the net effect is that the electron drift velocity saturates, becoming approximately independent of electric field (25). This saturation typically occurs for fields in the neighborhood of 1 kV/cm and in argon-based mixtures results in a velocity of about 5 cm/μs. The saturation of the electron drift velocity is an important advantage for drift-chamber operation (discussed later), since it reduces the sensitivity of the position measurement to operating conditions.

Development of the Avalanche Signal. As the electrons approach the anode wire, the electric field increases inversely as the distance to the wire. Above an electric-field threshold whose value depends on the gas, the electrons are accelerated

between collisions to sufficient energy that they can ionize a gas molecule on their next collision. Subsequently, the produced electrons (along with the initial electron) are accelerated and produce further ionization. An avalanche multiplication of charge rapidly develops, with gain typically in the range 10^4 to 10^6 electron–ion pairs per initial electron. Unlike the case of Geiger tubes and spark chambers, in proportional and drift chambers the avalanche is normally not allowed to grow into a spark but remains proportional in size to the amount of energy lost by the particle. The avalanche develops essentially instantaneously (in a time interval less than 1 ns) within a few wire diameters of the anode.

The time development of the anode-current pulse is determined by the increasing separation of the electron–ion pairs generated in the avalanche. Using Green's reciprocity theorem (26), and assuming the anode is connected to a low-input-impedance amplifier, one can show that the increment dq of induced charge on the anode due to the vector displacement $\boldsymbol{dr}$ of a charge Q between the two electrodes is given by

$$dq = \frac{Q}{V_0}\boldsymbol{E} \cdot \boldsymbol{dr} \tag{4}$$

where V_0 is the anode–cathode potential difference and $\boldsymbol{E}$ the electric field. [For cases with more than two electrodes, a more general result can be obtained from the weighting-field method (27).] At the instant of the avalanche, the electrons are collected on the anode, giving rise to a sharp initial current pulse. However, since the electrons are produced very near the anode, this initial pulse represents only a few percent of the total signal charge. Thus it is the slow drift of the positive ions from anode to cathode that provides most of the signal charge and determines the subsequent pulse development. [It should be noted that this imbalance between electron and ion contributions to the signal is specific to the cylindrical proportional-tube geometry with thin anode wire. In a parallel-plate geometry (28), the electrons contribute a much larger fraction of the signal charge.]

Multiwire Proportional Chambers. In order to register the positions of many particles spread over some area, one might employ a hodoscope made of individual proportional tubes. In the simplest approach, the true position of the particle is then approximated by the location of the wire that produces the pulse, that is, measured positions are "quantized" in units of the distance between adjacent anode wires. Proportional-tube hodoscopes have long been common in large-area, low-resolution applications such as muon detection (7,29), and have lately become popular in high-rate applications as the straw-tube array (30). However, a more common arrangement (which minimizes the detector material by eliminating the tube walls) is a multiwire proportional chamber (MWPC), consisting of a planar array of anode wires sandwiched between two cathode foils or grids. Although in such a device the electric field near the cathodes approximates a parallel-plate configuration, close to an anode wire the field shape resembles that in a proportional tube (see Fig. 2). The instrumentation of this detector usually involves individual signal detecting and coincidence/memory circuits for each anode wire.

The strength of the MWPC is its ability to handle a high flux of particles while providing good position resolution over a large detector area. Rates above 10^6 particles per $\text{cm}^2 \cdot \text{s}$ have been achieved (31) while maintaining greater than 95% detection efficiency. The rate capability of an MWPC is a strong function of the anode-wire spacing and the anode–cathode gap width, both of which should be as small as possible for high-rate operation. The statistics of the primary ionization described in Eq. (3) implies a minimum anode–cathode gap of a few millimeters for efficient particle detection (i.e., for the probability of no ionization to be negligibly small). In large detectors the anode-wire spacing and anode–cathode gap are limited by electromechanical instabilities (32). Thus large MWPCs (anodes exceeding about 1 m in length) have typical anode spacing of a few millimeters, while for anode length under 10 cm, spacing down to 0.5 mm is feasible. The anode-wire spacing w determines the rms position resolution σ of an MWPC according to

$$\sigma = \sqrt{\frac{1}{w}\int_{-w/2}^{w/2} x^2\,dx} = \frac{w}{\sqrt{12}} \tag{5}$$

This resolution is not always achievable due to the interplay between the pattern-recognition software and the occurrence of clusters of two or more wires registering hits for a single incident particle. Such hit clusters can arise when two adjacent wires share the ionization charge due to a track passing halfway between them, when several adjacent wires share the charge due to an obliquely inclined track, or when an energetic "knock-on" electron (also known as a δ ray) is emitted at a large angle by the incident particle and traverses several adjacent wires. When the best position resolution is required a proper treatment of hit clusters is necessary, but not always possible, leading to inefficiencies in the track reconstruction.

Two shortcomings of the MWPC in measuring particle positions are that the anode plane measures only one position coordinate (the one perpendicular to the wire length), and that the measured positions can assume only those values corresponding to anode–wire positions. For minimum-ionizing particles, a common way to provide information in the perpendicular coordinate direction (i.e., the distance along the wire) is to employ several anode planes, each oriented at a different angle, thus viewing the particle trajectory in "stereo"

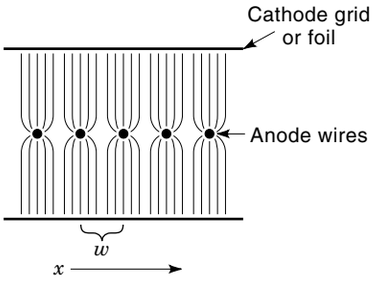

Figure 2. Sketch of the electric-field configuration in a multiwire proportional chamber. The anode wires are seen end-on. Close to the anode wire the field lines are radial as in a proportional tube, while close to the cathode planes the field lines are parallel as in a parallel-plate capacitor. The presence of a signal on an anode wire determines the position of the particle along the x axis in units of the anode-wire spacing w.

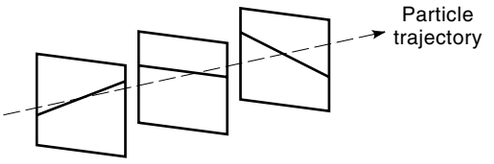

Figure 3. Schematic illustration showing how track positions in two dimensions are determined from measurements in three successive MWPCs with anode wires at three different angles; in each MWPC plane, only the wire producing a pulse is shown. Two stereo views would be sufficient in principle, but the third view helps to resolve ambiguities when more than one particle is being measured simultaneously.

(Fig. 3). In a multiple-particle event, a software algorithm is then required to match up the signals corresponding to each particle in the various views. In X ray detection another method must be used, since X rays interact in the gas via the photoelectric effect and are thereby absorbed, leaving a signal in only one plane. A technique for two-dimensional position measurement using only a single anode plane is charge division (33) in which the ratio of charges flowing out the two ends of a resistive anode wire specifies the position of the avalanche along the wire. However, in practice this technique yields only modest resolution (about 1% of wire length).

Cathode Readout of Proportional Chambers. Another technique for two-dimensional measurement of particle position using only one plane of anode wires is cathode readout. Cathode readout also improves position resolution by allowing interpolation between anode wires.

When an avalanche occurs on an anode wire, the pulse induced on the cathode planes carries information about the avalanche location. If the cathode planes are segmented and the charge induced on each segment digitized, the avalanche location can be accurately determined from the center-of-gravity of the charge distribution. The simplest arrangement is that of cathode-strip planes. To obtain two-dimensional information, one cathode plane can have strips oriented perpendicular to the wire direction (illustrated in Fig. 4), and the other can have strips parallel to the wires. Computation of the center of gravity can be performed either "off-line" after the signals have been digitized or "on-line," for example, via the transformation of signals from the spatial domain to the time domain using a specially patterned cathode (34). The accuracy of such delay-line position sensing is, in principle, independent of wire length.

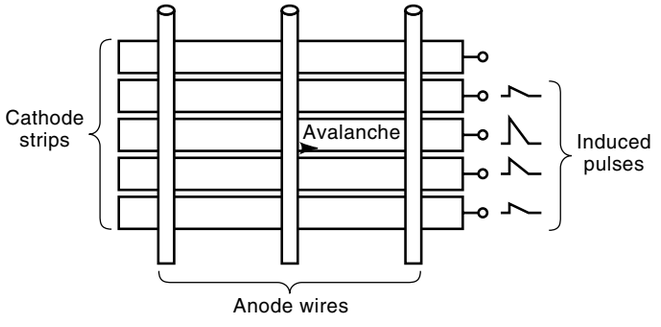

Figure 4. Schematic illustration of MWPC cathode-readout principle. (Dimensions are not to scale but are exaggerated for clarity.) The charges induced on the cathode strips, combined with the signals on the anode wires or on a second cathode plane (not shown) with strips parallel to the wires, allow localization of the avalanche in two dimensions.

For cathode strips perpendicular to the wires, there is a small nonlinearity in position measurement due to the finite strip width (35). This effect can be mitigated to some extent using specially shaped segmentation patterns (36). For cathode strips parallel to the wires, the measured position is modulated by the discrete positions of the wires around which the ions are created. However, at gains low enough that the avalanche remains in the proportional regime, the angular spread of the avalanche around the wire is limited (37), allowing some interpolation between the wires (38). Typically the position resolution along the wire is of order 100 μm and that perpendicular to the wire approximately five times worse.

The accuracy of the center-of-gravity method for cathode readout measuring the coordinate along the wire is at least an order of magnitude better than that of resistive charge division (for a given signal charge). For the coordinate perpendicular to the wire the electron-drift timing technique discussed in the next section is superior except when (as in X-ray detection) a timing reference is not available. The disadvantages of cathode readout are that it requires a large number of well-calibrated electronic channels and that one is still faced with the problem of correlating the coordinate pairs in a multiple-particle event. However, the latter problem is mitigated by the availability of a charge "signature." Due to the large dynamic range of primary ionization energy, cathode pulses from different particles will tend to differ in total charge, while pulses from the same particle will be correlated in total charge in the two views.

Drift Chambers. One drawback of the MWPC is the large number of anode wires and associated readout circuits needed to give fine position resolution over a large area. Drift chambers can substantially reduce the wire and electronics-channel counts. However, the generally wider anode spacing reduces rate capability, and the need for time measurement increases the electronic complexity of each channel.

The idea is to record not only the position of the wire closest to the particle trajectory, but also the distance of the particle from that wire, as measured by the time taken for the ionization electrons to drift along the electric-field lines in to the wire. One thus records the time of occurrence of the avalanche relative to some reference time tied to the passage of the particle. For minimum-ionizing-particle detection, the reference time can be provided by a signal from a scintillation counter. Given the known drift velocity of the electrons, the drift time determines the distance from the anode wire to an accuracy (typically 100 μm to 200 μm) primarily limited by diffusion of the drifting electrons in the gas. (In special cases, such as high pressure or specially tailored gas mixtures, the diffusion contribution can be reduced so that the contribution from δ rays becomes the limiting factor, allowing sub-100 μm accuracy.)

In a drift chamber the cathode planes are usually formed by wires at "graded" potentials, to provide a constant electric field for the drifting electrons (Fig. 5). Use of a gas mixture having a saturated drift velocity reduces the dependence of the position measurement on field inhomogeneities and operating conditions. As in an MWPC, a single anode plane of a

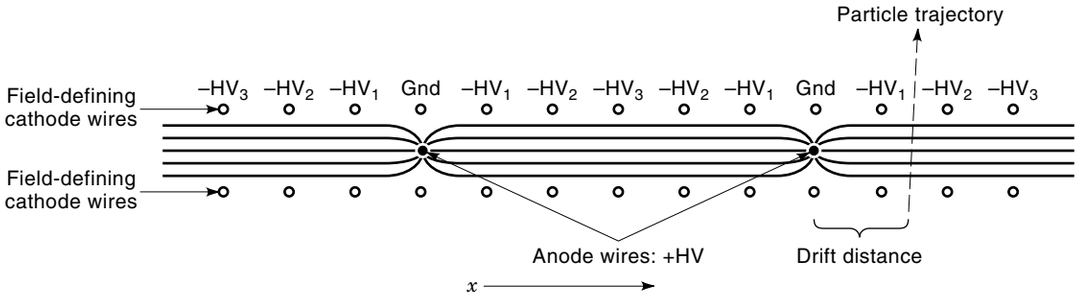

Figure 5. Sketch of the electric-field configuration in a drift chamber with "graded" cathode potentials. Wires are shown end-on. The anode plane is sandwiched between two planes of cathode wires whose high voltages (HV_1, HV_2, HV_3) with respect to ground potential (Gnd) are stepped to produce an approximately constant drift field.

drift chamber measures only the particle coordinate perpendicular to the wire direction. However, there is a twofold (so-called *left–right*) drift-direction ambiguity, which can be resolved by using several planes of anode wires with positions staggered so as not to lie parallel to a possible particle trajectory. Although not often done, the left–right ambiguity can also be resolved using the asymmetry of induced charge on nearby electrodes mentioned earlier, assuming the avalanche is sufficiently localized in azimuthal angle around the anode (39). The particle coordinate along the anode wire can be obtained through similar means as in an MWPC: additional stereo-view planes, charge division, or induced cathode signals. Since for drift chambers, position resolution is decoupled from anode-wire spacing, larger wire spacing than in MWPCs is typically used, making them more straightforward to construct and operate.

Time-Projection Chambers. A time-projection chamber (TPC) (40) is a gas-filled chamber in which ionization electrons produced along the path of a charged particle drift over a substantial distance (several centimeters to meters) before avalanching and being detected in an array of wire grids. With two-dimensional position measurement (e.g., anode and cathode readout), the entire particle trajectory through the chamber is recorded, with the third dimension "projected" into drift time. Such detectors are suitable when the average time between events is sufficiently long compared to the drift time. They are also beneficial when it is desirable to identify particles via their dE/dx ionization energy loss as discussed earlier.

Electronics for Proportional and Drift Chambers. Radeka (41,42) has analyzed the noise and resolution considerations in amplifiers for proportional chambers. Special operating conditions, such as high rates, bring additional concerns, some of which are discussed in Ref. 43. Since the majority of the signal charge stems from the slow motion of the positive ions liberated in the avalanche, one can use Eq. (4) to show that the signal current has the form (44)

$$i(t) \propto \frac{1}{1 + t/t_0} \tag{6}$$

assuming that the ions drift within a radial electric field directed outward from the anode. The characteristic time constant t_0 (of the order of 1 ns) depends on ion mobility, the electric-field strength at the anode, and the anode-wire diameter. In high-rate applications it is desirable to cancel the slow "$1/t$ tail" in order to be ready for another incident particle as quickly as possible. To do this, elaborate pulse-shaping circuits are sometimes employed using multiple pole–zero filters (43). With well-designed amplifiers and pulse shapers, typical double-pulse resolution of about 100 ns is feasible. When designing such a circuit, one should keep in mind that fluctuations (due to the arrival at the anode of individual ions) with respect to the average pulse shape make perfect pulse-shaping impossible. One must also consider that the amplifier is to be connected to a wire operated at kilovolt potential with respect to a surface that may be only a few millimeters away. While sparks are highly undesirable and may even break a wire, their occurrence cannot be ruled out. Thus amplifiers should be provided with adequate input protection.

In typical MWPC or drift-chamber operation, the amplifier output (or the output of a separate pulse-shaping circuit if used) is conveyed to a *discriminator* (a comparator driving a one-shot multivibrator) to produce a logic pulse when an input exceeding threshold occurs. The discriminator output may be used to set a latch in coincidence with a reference (*gate*) signal, as is typically done in MWPC installations. The readout circuitry then provides a list of wires having signals within the time interval of the reference signal. In drift-chamber operation one also needs to know the drift time of the ionization electrons; in this case the time interval between the discriminator output and the reference signal must be digitized. If cathode readout is desired, the pulse heights on all cathode segments must also be digitized.

The amplifier, pulse shaper, and discriminator may all be on separate multichannel circuit boards, combined on one or two circuit boards, or even all combined into a single hybrid or integrated circuit. Since for high-rate applications these circuits need to have both large gain and large bandwidth, and each is connected to an imperfectly shielded antenna (the anode wire), stabilizing large installations against parasitic oscillation is usually challenging and requires careful attention to grounding and circuit and detector layout.

Readout of the induced signals on cathodes usually requires longer shaping time and hence less bandwidth. This is primarily due to the longer time required for development of the cathode signal, since the induced cathode charge increases as the ions drift away from the screening influence of the nearby anode wire. Nevertheless, since the accurate

computation of the center of gravity requires a large dynamic range, to guard against electromagnetic interference and cross-talk, the cautions just mentioned concerning system layout apply here as well.

Solid-State Detectors

Silicon-strip detectors (45) have come into increasing use for tracking applications near the interaction vertex, where tracks are close together and precise position measurements are needed. These detectors are multiple-diode structures fabricated on single wafers of high-resistivity silicon and operated under reverse bias. A center-to-center distance between adjacent strips as small as 10 μm (25 μm to 50 μm is common) allows position resolution an order of magnitude better than that of drift chambers. The resolution achieved depends on readout mode: With single-bit-per-strip digital readout (as for MWPCs) the resolution is as given in Eq. (5), while if analog pulse-height information is used, interpolation between strips is possible because of charge spreading over adjacent strips; then rms resolution of a few microns can be achieved.

A charged particle traversing silicon creates electron–hole pairs from ionization energy at the rate of one pair per 3.6 eV. With typical 300 μm detector thickness, the signal is about 25,000 electrons, an order of magnitude smaller than in a proportional chamber. However, the reduced capacitance of a silicon strip and its associated readout electronics compared to that in an MWPC can allow improved noise performance. This is especially true for the recently developed silicon pixel detectors (46–48), in which an individual diode can have dimensions of 30 μm $\times$ 300 μm or less. Compared to strip detectors, pixel detectors also offer ease of track reconstruction, since the firing of a pixel determines a point in space along the particle trajectory rather than a line segment. To achieve efficient and rapid charge collection from the full thickness of the detector requires fully depleting the diodes, leading to typical operating voltage of about 100 V. The signal out of the n-type side then develops in a few nanoseconds (49). With fast shaping time, extremely high particle rates (of order MHz per strip or pixel) can thus be handled, the limit to rate capability being radiation damage to the detectors and electronics over the long term.

Charged-coupled devices (CCDs) have also been employed for space-point tracking close to the vertex (50). To achieve adequate signal-to-noise ratio they must be operated with cryogenic cooling. CCDs have the virtue of good position resolution ($<$10 μm rms) in both dimensions, at the expense of long (of order 100 ms) readout time. They are thus not well suited to high-rate experiments.

Other materials have been considered for strip and pixel particle-position measurement. At present much development effort is focused on the problem of radiation damage in vertex detectors (51), since silicon detectors commonly become unusable after a few megarad of irradiation. Due to their larger band gaps, materials such as GaAs (52) or diamond (53) should be substantially more radiation-hard than silicon; however, they feature worse signal-to-noise ratio.

Reverse-biased silicon (and germanium) detectors and CCDs are also in widespread use for X-ray and synchrotron-radiation detection (2), nuclear physics, etc.

Amplifiers and signal-processing circuitry for silicon-strip and pixel detectors present challenges to the designer since the small feature size of the detector implies very large channel counts (of order 10^5 strips or 10^8 pixels) in an experiment. The cost per channel is thus a key design criterion, and, since the circuits often need to be packed into a small volume, so also are circuit size, interconnections, and power dissipation. Various implementations have lately been developed as semicustom (54) and full-custom integrated circuits (55). Pixel detectors necessarily require custom very-large-scale integrated circuit (VLSI) readout electronics, either integrated onto the detector chip itself (47) or as a separate chip bump-bonded to the detector chip (48).

Calorimeters

Two common types of calorimeter are those optimized for the detection of electrons and photons (designated *electromagnetic*) and those optimized for strongly interacting particles (designated *hadronic*). Another important distinction is whether the output signal is proportional to all of the deposited energy or to only a portion of it; in the latter case the calorimeter is of the *sampling* type.

Sampling Calorimeters. A common arrangement for a sampling calorimeter is a sandwich consisting of layers of dense material interspersed with particle detectors such as scintillation counters. Such a calorimeter can be electromagnetic or hadronic depending on the dense material chosen. Often a combined electromagnetic–hadronic device is built, consisting of an initial electromagnetic section using lead plates followed by a hadronic section using iron plates. Lead's short radiation length (0.56 cm) combined with its long (17 cm) mean free path for hadronic interaction means that electrons and hadrons can be well discriminated in such a structure. Electrons interact in the lead producing an electromagnetic shower as they radiate bremsstrahlung photons that produce electron–positron pairs that in turn radiate photons, etc. Almost all of the electron's energy is thus deposited in the electromagnetic section, which is typically about 20 radiation lengths thick. In a well-designed calorimeter, the ionization energy deposited by the shower of electrons and positrons in the interspersed scintillator ("active") layers is proportional to the energy of the incident electron to good approximation. Most hadrons pass through the electromagnetic section leaving only ionization energy and proceed to interact strongly, producing a hadronic shower, in the iron plates of the hadronic section.

Energy measurement in sampling calorimeters is limited in resolution due to statistical fluctuations in the ratio of the energy deposited in the active layers to that in the inactive layers. The percent resolution is inversely proportional to the square root of the deposited energy. Typical performance for electromagnetic showers is relative rms energy uncertainty $\sigma(E)/E = 10\%/\sqrt{E}$ ($75\%/\sqrt{E}$ for hadronic), where E is expressed in GeV. At the highest energies, as this quantity goes to zero, other contributions (for example, calibration uncertainties) dominate. It is difficult to measure energy in sampling calorimeters to better than a few percent.

The poor energy resolution of hadronic sampling calorimeters arises from random fluctuations in the shower composition (e.g., in the relative numbers of neutral versus charged pions produced) and from energy-loss mechanisms (such as breakup of nuclei in the inactive layers) not yielding signal in the sampling medium. The decay of the neutral pion into a

pair of photons converts hadronic energy into electromagnetic energy, which degrades the energy resolution due to the differing response to electromagnetic and hadronic energy. In *compensating* calorimeters, design parameters are tuned to minimize this response difference and thereby optimize hadronic energy resolution (56).

Techniques for calibrating calorimeters include injecting light using lasers as well as studying the response to high-energy muons. Since muons do not shower, they deposit only minimum-ionizing pulse height in the active layers. The need to measure with precision both muons and showers leads to stringent demands for analog-to-digital-converter linearity and dynamic range (57); 14 bits is not uncommon.

Homogeneous Calorimeters. These include the inorganic scintillators discussed earlier as well as lead-glass arrays and liquid-argon and liquid-xenon ionization chambers. Lead glass is not a scintillator, but electrons and positrons from an electromagnetic shower occurring within it emit visible Cherenkov light that can be detected using PMTs. Since they are not subject to sampling fluctuations, homogeneous electromagnetic calorimeters generally have better energy resolution than sampling calorimeters, for example, the $2.7\%/E^{1/4}$ (FWHM) that was achieved by the Crystal Ball collaboration using thallium-doped sodium iodide (58) and the $5\%/\sqrt{E}$ achieved by the OPAL collaboration using lead glass (59).

PARTICLE SPECTROMETERS

Particle spectrometers are characterized by great variety in their purposes and layouts. Generically they may be divided into fixed-target spectrometers, in which a beam is aimed at a target that is stationary (or in the case of a gas-jet target, moving slowly) in the laboratory, and colliding-beam spectrometers, in which two particle beams moving in opposite directions are brought into collision. We consider next two typical examples to illustrate the use of the detectors and techniques described previously.

The Fermilab HyperCP Spectrometer

As a simple example of a fixed-target spectrometer we consider that of the Fermilab HyperCP experiment (Fig. 6). The goal of the experiment is the precise comparison of decays of Ξ^- baryons (quark content *ssd*) with those of $\overline{\Xi}^+$ antibaryons ($\overline{ssd}$), in order to search for a postulated subtle difference between matter and antimatter. The difference in properties between matter and antimatter has been observed through the behavior of only one particle type to date (the neutral kaon). Nevertheless, it is believed to be a general feature of the fundamental interactions among elementary particles and, furthermore, to be responsible for the dominance of matter over antimatter in the universe (60).

Baryons containing strange quarks are known as hyperons. The Ξ^- and $\overline{\Xi}^+$ hyperons are produced by interactions of 800 GeV *primary* protons from the Fermilab Tevatron accelerator in a small metal target upstream of the *Hyperon* magnet (Fig. 6). That magnet is filled with brass and tungsten shielding, into which a curved channel has been machined such that charged particles of momenta in the range 125 to 250 GeV/c traverse the channel and emerge out the end to form the *secondary* beam, while neutral particles and charged particles outside that momentum range curve either too little or too much and enter the shielding, where they shower and are absorbed. The field directions in the hyperon and analyzing magnets can be set to select either Ξ^- or $\overline{\Xi}^+$ events.

Figure 7 shows the momentum distribution of charged particles emerging from the channel in the positive-beam ($\overline{\Xi}^+$) setting. Note that this distribution arises classically, not quantum-mechanically: To accept only a single value of momentum the channel would need to be infinitesimally narrow. Since its width is finite, it in fact accepts particles over some range of track curvature and momentum.

The Ξ^- or $\overline{\Xi}^+$ hyperon undergoes "cascade" decay as each strange quark decays in turn via the weak force. As indicated in Fig. 6(b), the Ξ^- can decay into a Λ^0 hyperon and a negative pion, and the Λ^0 can decay into a proton and a negative pion. It is this decay chain that the HyperCP experiment studies. The events of interest thus contain a proton (or antiproton) of one charge and two pions of the opposite charge. (For simplicity, Ξ^- and $\overline{\Xi}^+$ are generically referred to simply as Ξ in the following discussion, and Λ^0 and $\overline{\Lambda}^0$ as Λ.)

Triggering and Data Acquisition. The pion and proton hodoscopes (Fig. 6) are arrays of vertical scintillation counters used to trigger data acquisition from the spectrometer. A trigger signal is created whenever counts are detected simultaneously in both hodoscopes and in the hadronic calorimeter. The state of all detector elements is then digitized and recorded on magnetic tape for later computer analysis. The role of the calorimeter is to suppress triggers that could occur when ambient muons or other low-energy particles count in the hodoscopes. Large numbers of such background particles are produced by particle interactions in the shielding, but their contribution to the trigger rate is effectively suppressed by the calorimeter trigger requirement. The 100 kHz rate of event triggers is dominated by interactions of secondary-beam particles in the material of the spectrometer that give counts in both hodoscopes.

The HyperCP data acquisition system (61) has the highest throughput of any currently in use in high-energy physics. Digitization of event information typically is completed in less than 3 μs, giving average "live time" (the fraction of time that the system is available to process triggers) of about 70% at 100 kHz trigger rate. To minimize the amount of information that must be recorded to describe each event, the spectrometer design was kept as simple as possible, resulting in an average "event size" of just 580 bytes. Nevertheless, the average data rate is about 15 Mbyte/s and is streamed to 40 magnetic tapes in parallel by 15 single-board computers housed in five VME crates. (Since in fixed-target operation beam is extracted from the Tevatron for only about 20 s each minute, the data acquisition rate from the digitizing system is about three times the average rate to tape, with a 960 Mbyte buffer memory providing temporary data storage.)

Coordinate Measurement. The trajectories of charged particles in the spectrometer are measured using a telescope of multiwire-proportional-chamber modules (C1 to C8). Since the channeled secondary-beam rate exceeds the rate of Ξ decays by a factor greater than 10^4, the rate capability of the these detectors is key to obtaining the desired large sample (of order 10^9 events) of hyperon and antihyperon decays. To maximize rate capability, 1 mm anode-wire-spacing MWPCs

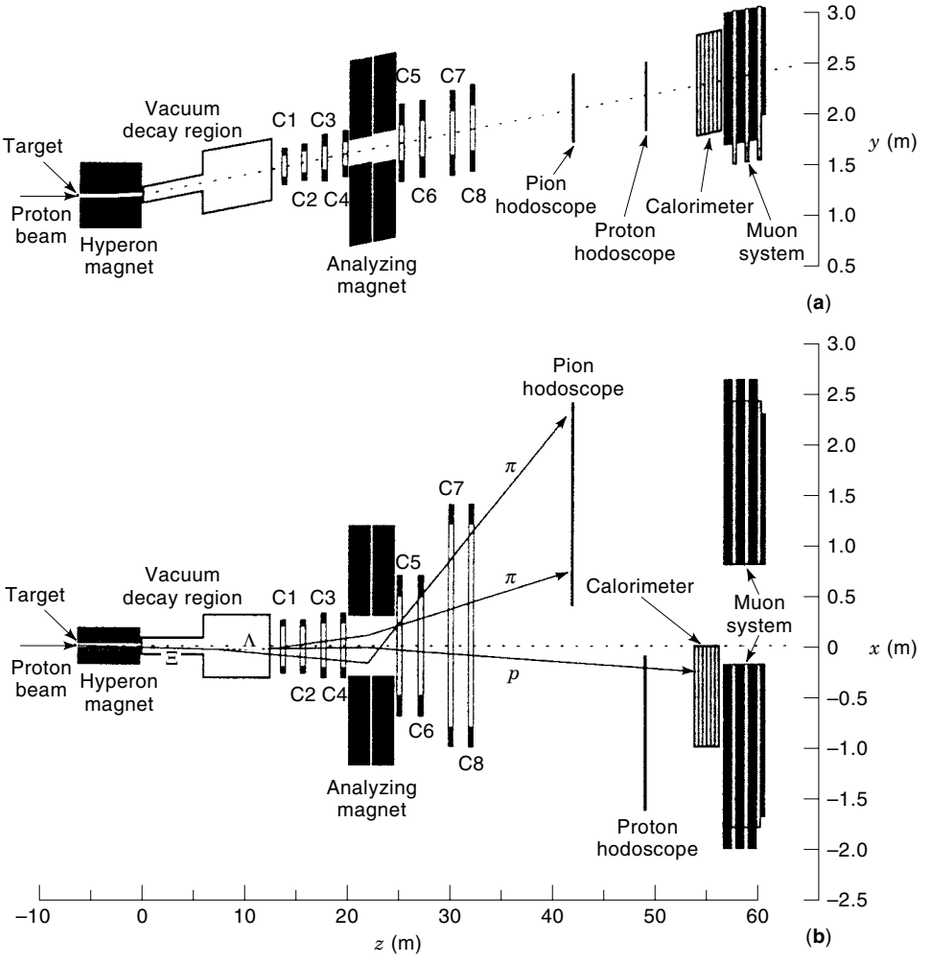

Figure 6. (a) Elevation and (b) plan views of the Fermilab HyperCP spectrometer. (Note the different horizontal and vertical distance scales.) Typical particle trajectories are shown for a cascade decay $\Xi \rightarrow \Lambda\pi$, $\Lambda \rightarrow p\pi$. For graphical simplicity, the curvature of the charged-particle tracks within the analyzing magnet is approximated by a single sharp bend.

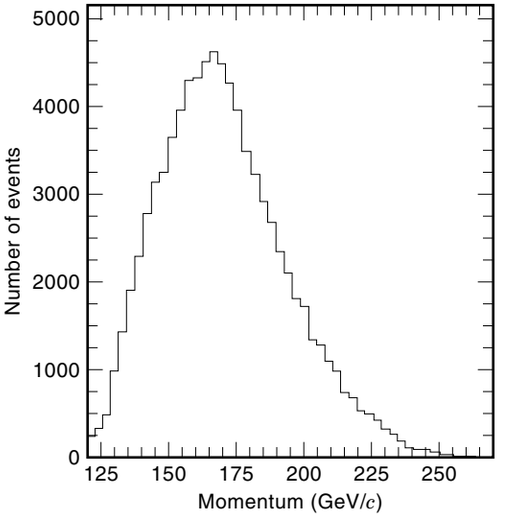

Figure 7. Charged particles emerging from the HyperCP hyperon channel have momenta distributed about a mean value of about 170 GeV/c.

are employed for modules C1 and C2, with wire spacing ranging up to 2 mm for modules C7 and C8. With a gas mixture of 50% CF_4–50% isobutane, module C1 (which experiences the highest rate per unit area) operates reliably at a rate exceeding 1 MHz/cm^2.

To measure the particle positions in three dimensions, more than one measurement view is required. Each of the eight chamber modules contains four anode planes, two of which have vertical wires and two of which have wires at angles of $\pm 27°$ with respect to the first two. This choice of stereo angle is found to optimize the measurement resolution for hyperon mass and decay point. Measurements are thus provided in x as well as in directions rotated by $\pm 27°$ with respect to x, from which y coordinates can be computed. z coordinates are given by the known locations of the MWPC planes.

Event Reconstruction. Given the information from the MWPC telescope, three-dimensional reconstruction of the momentum vector of each charged particle can be carried out on a computer. Since momentum is conserved, the vector sum of the momenta of the Ξ decay products must equal the momentum vector $\boldsymbol{p}_\Xi$ of the Ξ itself, and likewise, since energy is conserved, the sum of the energies of the decay products must

equal the energy E_Ξ of the Ξ. From the relativistic relationship among mass, energy, and momentum, the mass of the Ξ can be reconstructed as

$$m_\Xi c^2 = \sqrt{E_\Xi^2 - p_\Xi^2 c^2} \tag{7}$$

This calculation requires knowledge of the energies of the Ξ^- decay products. To calculate the energy of a decay product from its momentum, its mass must be known. While the masses could be determined using Cherenkov counters, we will see later that in this instance it is sufficient simply to assume that the two equal-charged particles are pions and the particle of opposite charge is the proton or antiproton. Of course, these assumed particle identities are not always correct, nor are all observed combinations of a proton (or antiproton) and two negative (or positive) pions in fact decay products of a Ξ^- (or $\overline{\Xi}^+$).

Figure 8 shows the distribution in mass of a sample of $\bar{p}\pi^+\pi^+$ combinations from the HyperCP experiment. A clear peak at the mass of the $\overline{\Xi}^+$ is evident, superimposed on a continuum of background events in which the assumed particle identities are incorrect. The width of the peak reflects uncertainties in the measurement of the particle momentum vectors. These arise from the wire spacings of the MWPCs and from multiple scattering of the particles as they pass through the material of the detectors (again an example in which the measurement uncertainty is not quantum-mechanically dominated). By requiring the reconstructed mass to fall within the peak, one can select predominantly signal events and suppress background. The signal-to-background ratio can be improved by carrying out constrained fits to the cascade decay geometry and constraining the momentum vectors of the Λ decay products to be consistent with the known Λ mass. While the signal-to-background ratio could be further improved by using Cherenkov counters for particle identification, the improvement would come at the expense of increased cost, complexity, and event size and is not needed for the purposes of the experiment.

Also of interest in the HyperCP experiment is the distribution in the decay point of the Ξ hyperons. This is shown in

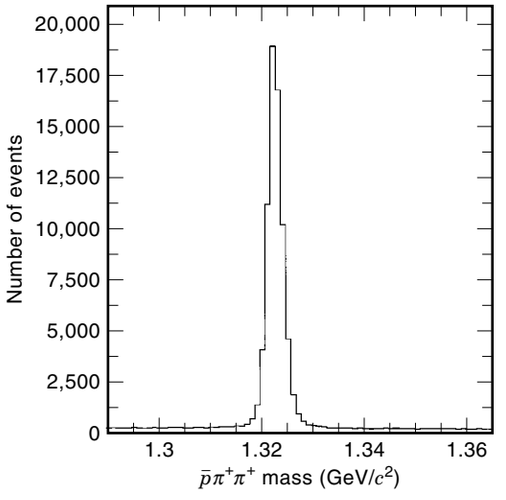

Figure 8. Distribution in mass of a sample of $\bar{p}\pi^+\pi^+$ combinations from the HyperCP experiment.

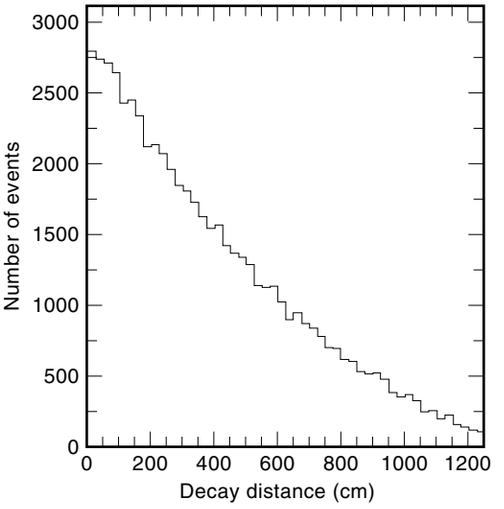

Figure 9. Distribution in decay distance of a sample of $\overline{\Xi}^+ \to \overline{\Lambda}\pi^+ \to \bar{p}\pi^+\pi^+$ combinations from the HyperCP experiment. To enhance the signal relative to the background, the $\bar{p}\pi^+\pi^+$ mass is required to fall within ± 5 MeV/c^2 of the known $\overline{\Xi}^+$ mass.

Fig. 9. The Ξ decay point is reconstructed for each event by first locating the point of closest approach of the Λ decay products. This point represents the position at which the Λ decayed. The Λ trajectory is then extrapolated upstream to its point of closest approach with the pion track from the Ξ decay, which represents the position at which the Ξ decayed. We observe an (approximately) exponential distribution as expected for the decay of an unstable particle. This reflects quantum-mechanical randomness: although the Ξ has a definite *average* lifetime (as given in Table 2), the actual time interval from creation to decay of a given individual Ξ cannot be predicted but varies randomly from event to event. The deviations from exponential character arise from three sources: (1) some background events are present in the sample, (2) we have not corrected for the (momentum-dependent) relativistic time-dilation factor γ, which is different for each event, and (3) the detection probability is not entirely uniform for Ξ hyperons decaying at different points within the vacuum decay region. These effects can all be corrected in a more sophisticated analysis, but the simple analysis presented here serves to illustrate the key points.

Collider Detector at Fermilab

To indicate the wide range of possible spectrometer configurations, we next consider briefly the Collider Detector at Fermilab (CDF) spectrometer. This is an example of a colliding-beam spectrometer notable for its use (along with the D0 spectrometer) in the 1995 discovery of the top quark. A key difference between fixed-target and colliding-beam spectrometers is that in the former case the reaction products emerge within a narrow cone around the beam direction, whereas two beams colliding head-on produce reaction products that emerge in all directions. This leads to rather different spectrometer layouts in the two cases. A typical design goal of colliding-beam spectrometers is *hermeticity,* that is, as few as possible of the particles produced in the collisions should escape undetected. This of course contradicts the requirements

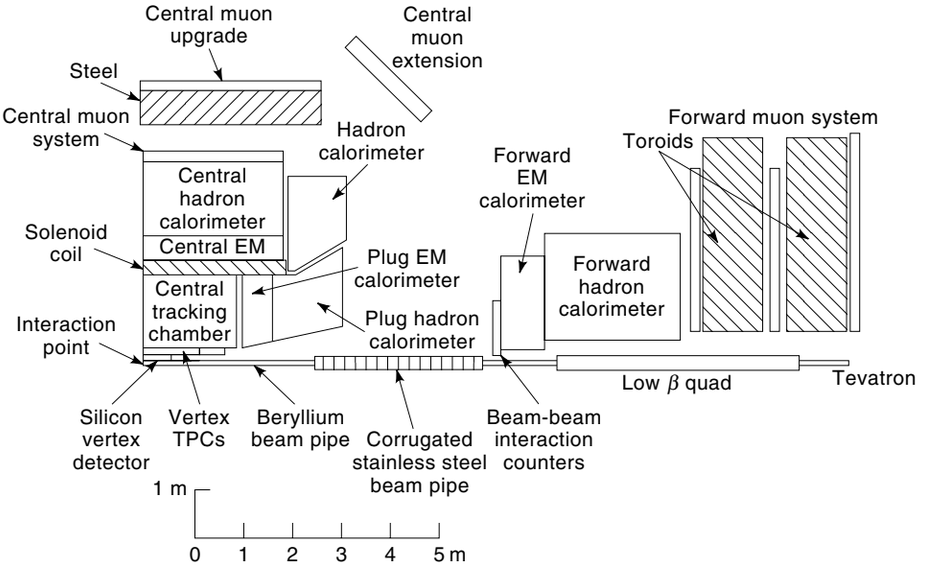

Figure 10. Schematic diagram of the Collider Detector at Fermilab spectrometer. One-quarter is shown; the rest is implied by rotational symmetry about the beam pipe and mirror symmetry about the plane through the interaction point perpendicular to the beam pipe.

that the detectors be supported in place and that the signals be brought out; thus compromises are necessary.

The CDF detector has been described in the literature (62); space constraints preclude a detailed discussion here. Figure 10 shows schematically one-quarter of the spectrometer, which surrounds the point (actually a region about 0.5 m long) inside the Tevatron beam pipe at which the proton and antiproton beams collide. Figure 11 shows the actual layout. Figure 12 is an *event display,* that is, a schematic diagram showing the particle tracks as reconstructed by the spectrometer; the event shown contains a high-momentum muon (μ^-) and antimuon (μ^+) resulting from the production and decay of a Z^0 gauge boson. In the figure the beam axis runs into and out of the page, as does the magnetic field due to the super-

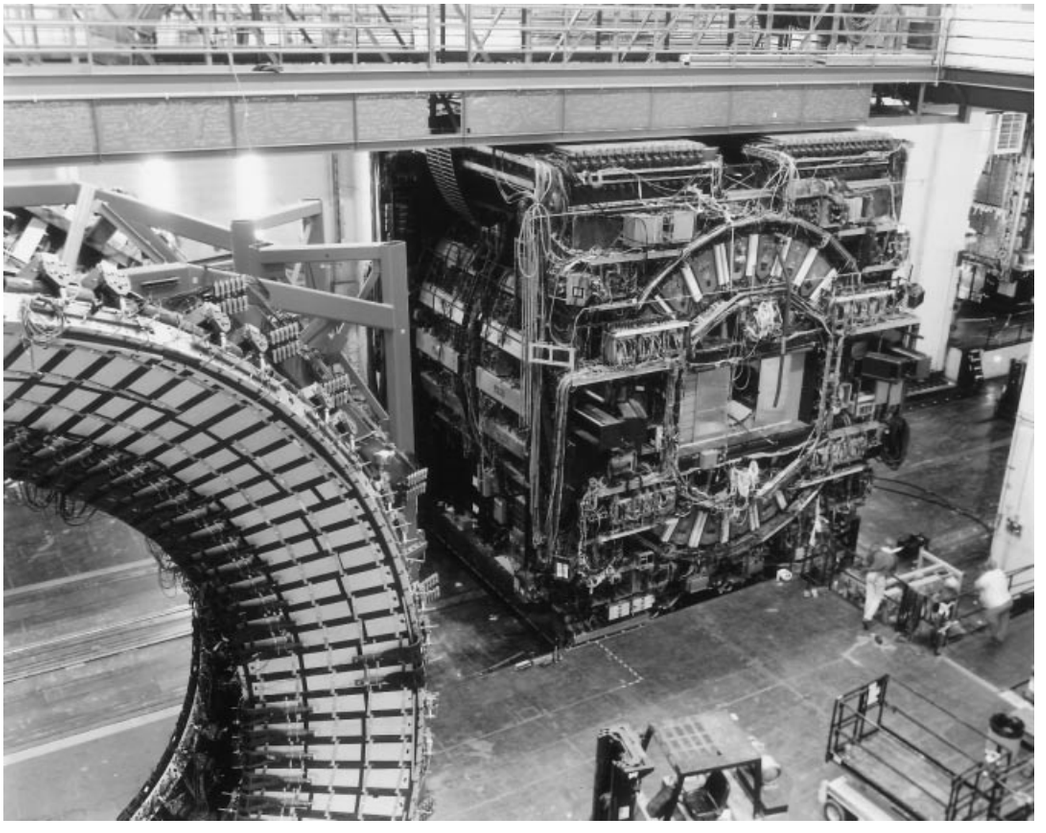

Figure 11. Photograph of the Fermilab Collider Detector Facility (CDF) spectrometer in its assembly hall; the forward detectors have been retracted to give access to the central portion.

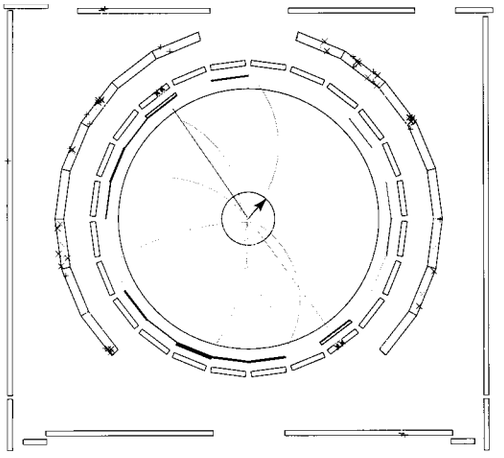

Figure 12. End-view display of a CDF event containing a $Z_0 \rightarrow \mu^+\mu^-$ decay. The muon tracks are the two line segments emerging back-to-back from the interaction point at about 5 o'clock and 11 o'clock. They are identified as muons by the ×'s that indicate signals in the inner and outer muon detectors. Because of their high momentum ($p_\mu = m_{Z^0}c/2 = 45.6$ GeV/c), the muon tracks show little curvature as compared to the tracks of the remaining (lower-momentum) charged particles in the event. It is apparent that more tracks point down and to the left than up and to the right, suggesting that noninteracting electrically neutral particles (neutrinos) may have been produced, or that some neutral particles were missed due to cracks in the calorimeters. The "missing momentum" vector due to the undetected neutral particles is indicated by the arrow. (The "low-B" quadrupole magnets serve to focus the proton and antiproton beams at the interaction point.)

conducting solenoidal momentum-analyzing electromagnet. The curvature of charged-particle tracks due to the magnetic field is clearly evident. A positive identification of a muon can be made for those trajectories that pass through the massive hadronic calorimeter relatively unscathed and leave signals in surrounding scintillators and wire chambers.

Figure 13 shows the distribution in muon-pair mass observed by the CDF detector. The prominent peak at 91 GeV/c^2 is due to the Z^0 boson. Its width reflects both the (classical) measurement resolution of the magnetic spectrometer and the (quantum-mechanical) uncertainty of the Z^0 boson's mass (intrinsic width $\Gamma = 2.49$ GeV/c^2 FWHM) due to its short lifetime. Since Γc^2 represents the Z^0 boson's energy uncertainty and the lifetime τ its duration uncertainty, they satisfy a version of the Heisenberg uncertainty relation: $\Gamma c^2 \tau = \hbar/2$.

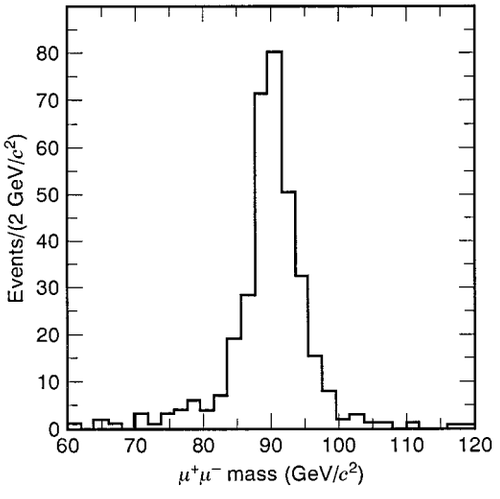

Figure 13. Dimuon mass spectrum obtained by the CDF collaboration.

SUMMARY

Following an introduction to particle physics and particle detectors, we have considered two contrasting examples of subatomic-particle spectrometers, ranging from the relatively simple (HyperCP) to the complex (CDF). While the brief discussion just given illustrates the variety of issues encountered in designing particle spectrometers and their electronic instrumentation, the actual design process is quite involved. Extensive computer simulation is generally employed to tailor a solution optimized for the problem at hand. Requirements for performance and reliability often come up against practical constraints on cost and on development and assembly time.

The ongoing development of new technology for particle detectors and their instrumentation, together with the development of increasingly intense particle beams, make measurements possible that were previously not feasible. When new detector technology is employed, simulation studies must be combined with prototype tests both on the bench and at test beams. The investigation of matter and energy at ever deeper and more sophisticated levels exemplifies fruitful collaboration among scientists and engineers.

ACKNOWLEDGMENTS

The authors thank N. Gelfand for useful discussions and the Particle Data Group and the Fermilab CDF and HyperCP collaborations for permission to reproduce their results. This work was carried out with support from the U.S. Department of Energy under Grants DE-FG02-94ER40840 and DE-AS05-89ER40518.

BIBLIOGRAPHY

1. M. Mandelkern, Nuclear techniques for medical imaging: Positron emission tomography, *Ann. Rev. Nucl. Part. Sci.,* **45**: 205–254, 1995.
2. E. M. Westbrook and I. Naday, Charge-coupled device-based area detectors, *Methods Enzymol.,* **276**: 244–268, 1997.
3. J. R. Janesick and S. T. Elliot, History and advancement of large area array scientific CCD imagers, *Astron. Soc. Pacific Conf. Series,* Tucson, AZ, 1991.
4. R. M. Barnett et al., (Particle Data Group), Review of particle physics, *Phys. Rev. D,* **54**: 1–720, 1996.
5. J. A. Appel et al., Performance of a lead-glass electromagetic shower detector at Fermilab, *Nucl. Instrum. Methods,* **127**: 495–505, 1975.
6. I. Gaines, Hadrons and leptons at high transverse momentum, Ph.D. thesis, Columbia Univ., 1976, p. 59.
7. T. Murphy et al., Hadron showers in iron and muon identification, *Nucl. Instrum. Methods A,* **251**: 478–492, 1986.
8. G. D'Agostini et al., *Nucl. Instrum. Methods A,* **219**: 495–500, 1984.

9. J. Litt and R. Meunier, Cerenkov counter technique in high-energy physics, *Annu. Rev. Nucl. Sci.,* **23**: 1–43, 1973.
10. J. Seguinot and T. Ypsilantis, A history survey of ring imaging Cherenkov counters, *Nucl. Instrum. Methods A,* **343**: 1–29, 1994; T. Ypsilantis and J. Seguinot, Theory of ring imaging Cherenkov counters, *ibid.,* **343**: 30–51, 1994.
11. B. Dolgoshein, Transition radiation detectors, *Nucl. Instrum. Methods A,* **326**: 434–469, 1993.
12. KTeV Collaboration, E. Cheu et al., Proposal to continue the study of direct CP violation and rare decay processes at KTeV in 1999, proposal to Fermilab, 1997 (unpublished).
13. The radiation lengths of various materials have been calculated and tabulated by Y. S. Tsai and can be found in the *Review of Particle Physics* (Ref. 4), p. 72.
14. R. K. Swank, Characteristics of scintillators, *Annu. Rev. Nucl. Sci.,* **4**: 111–140, 1954.
15. P. H. Eberhard et al., Detection efficiency and dark pulse rate of Rockwell (SSPM) single photon counters, in G. A. Lampropoulos, J. Chrostowski, and R. M. Measures (eds.), *Applications of Photonic Technology,* New York: Plenum, 1995, pp. 471–474.
16. C. R. Kerns, A high rate phototube base, *IEEE Trans. Nucl. Sci.,* **NS-24**: 353–355, 1977.
17. R. Ruchti, Scintillating fibers for charged-particle tracking, *Annu. Rev. Nucl. Sci.,* **46**: 281–319, 1996.
18. A variant of the solid-state photomultiplier described by M. D. Petroff and W. G. Stapelbroek, Photon-counting solid-state photomultiplier, *IEEE Trans. Nucl. Sci.,* **NS-36**: 158–162, 1989; M. D. Petrov, M. G. Stapelbroek, and W. Z. Kleinhans, Detection of individual 0.4–28 μm wavelength photons via impurity-impact ionization in a solid-state photomultiplier, *Appl. Phys. Lett.,* **51**: 406–408, 1987.
19. B. Baumbaugh et al., Performance of multiclad scintillating and clear waveguide fibers read out with visible light photon counters, *Nucl. Instrum. Methods A,* **345**: 271–278, 1994.
20. C. Bebek, A cesium iodide calorimeter with photodiode readout for CLEO-II, *Nucl. Instrum. Methods A,* **265**: 258–265, 1988.
21. G. Charpak et al., The use of multiwire proportional counters to select and localize charged particles, *Nucl. Instrum. Methods,* **62**: 262–268, 1968.
22. G. Charpak and F. Sauli, High resolution electronic particle detectors, *Annu. Rev. Nucl. Sci.,* **34**: 285–349, 1984.
23. J. Kadyk, Wire chamber aging, *Nucl. Instrum. Methods A,* **300**: 436–479, 1991; J. Wise, J. A. Kadyk, and D. W. Hess, A chemical model for wire chamber aging in CF_4/iC_4H_{10} gases, *J. Appl. Phys.,* **74**: 5327–5340, 1993.
24. H. Fischle, J. Heintze, and B. Schmidt, Experimental determination of ionization cluster size distributions in counting gases, *Nucl. Instrum. Methods A,* **301**: 202–214, 1991.
25. S. F. Biagi, A multiterm Boltzmann analysis of drift velocity, diffusion, gain and magnetic-field effects in argon-methane-water vapour mixtures, *Nucl. Instr. Methods A,* **238**: 716–722, 1989.
26. D. J. Griffiths, *Introduction to Electrodynamics,* 2nd ed., Englewood Cliffs, NJ: Prentice-Hall, 1989, p. 156.
27. S. Ramo, Currents induced by electron motion, *Proc. Inst. Radio Eng.,* **27**: 584–585, 1939; see also Ref. 42.
28. A. Peisert, The parallel plate avalanche chamber as an endcap detector for time projection chambers, *Nucl. Instrum. Methods,* **217**: 229–235, 1983.
29. C. Brown et al., D0 muon system with proportional drift tube chambers, *Nucl. Instrum. Methods A,* **279**: 331–338, 1989.
30. P. Baringer et al., A drift chamber constructed of aluminized mylar tubes, *Nucl. Instrum. Methods A,* **254**: 542–548, 1987.
31. J. Fischer et al., Proportional chambers for very high counting rates based on gas mixtures of CF_4 with hydrocarbons, *Nucl. Instrum. Methods A,* **238**: 249–264, 1985.
32. G. Charpak et al., Some features of large multiwire proportional chambers, *Nucl. Instrum. Methods A,* **97**: 377–388, 1971; R. Bouclier et al., Proportional chambers for a 50,000-wire detector, *ibid.,* **115**: 235–244, 1974.
33. V. Radeka and P. Rehak, Second coordinate readout in drift chambers by charge division, *IEEE Trans. Nucl. Sci.,* **NS-25**: 46–52, 1978.
34. A. R. Erwin et al., Operational experience with a 2.5×1.5 meter delay line chamber, *Nucl. Instrum. Methods A,* **237**: 493–500, 1985.
35. E. Gatti et al., Optimum geometry for strip cathodes or grids in MWPC for avalanche localization along the anode wires, *Nucl. Instrum. Methods,* **163**: 83–92, 1979.
36. E. Mathieson and G. C. Smith, Reduction of non-linearity in position-sensitive MWPCs, *IEEE Trans. Nucl. Sci.,* **NS-36**: 305–310, 1989.
37. T. J. Harris and E. Mathieson, Angular localisation of proportional chamber avalanche, *Nucl. Instrum. Methods,* **154**: 183–188, 1978.
38. G. Charpak et al., Progress in high-accuracy proportional chambers, *Nucl. Instrum. Methods,* **148**: 471–482, 1978.
39. G. Charpak, F. Sauli, and W. Duinker, High-accuracy drift chambers and their use in strong magnetic fields, *Nucl. Instrum. Methods,* **108**: 413–426, 1973.
40. D. R. Nygren, Future prospects of the TPC idea, *Phys. Scr.,* **23**: 584–589, 1981.
41. V. Radeka, Signal, noise and resolution in position sensitive detectors, *IEEE Trans. Nucl. Sci.,* **NS-21**: 51–64, 1974.
42. V. Radeka, Low noise techniques in detectors, *Annu. Rev. Nucl. Part. Sci.,* **38**: 217–277, 1989.
43. R. A. Boie, A. T. Hrisoho, and P. Rehak, Signal shaping and tail cancellation for gas proportional detectors at high counting rates, *Nucl. Instrum. Methods,* **192**: 365–374, 1982.
44. G. R. Ricker, Jr. and J. J. Gomes, Pulse risetimes in proportional counters, *Rev. Sci. Instrum.,* **3**: 227–233, 1969.
45. G. Hall, Semiconductor particle tracking detectors, *Rep. Prog. Phys.,* **57**: 481–531, 1994; G. Lutz and A. S. Schwarz, Silicon devices for charged-particle track and vertex detection, *Annu. Rev. Nucl. Part. Sci.,* **45**: 295–335, 1995.
46. T. Mouthuy, Silicon pixel detector research and development, *Nucl. Instrum. Methods A,* **368**: 213–216, 1995.
47. C. J. Kenney et al., A prototype monolithic pixel detector, *Nucl. Instrum. Methods A,* **342**: 59–77, 1994.
48. S. L. Shapiro et al., Silicon PIN diode array hybrids for charged particle detection, *Nucl. Instrum. Methods A,* **275**: 580–586, 1989; M. Campbell et al., Development of a pixel readout chip compatible with large area coverage, *Nucl. Instrum. Methods A,* **342**: 52–58, 1994.
49. A. Rudge and P. Weilhammer, A very high bandwidth low noise amplifier for Si detector readout, in *Proc. 3rd Int. Conf. Electron. Future Colliders,* Chestnut Ridge, NY: LeCroy Res. Syst., 1993, pp. 181–197.
50. M. G. Strauss (for the SLD Collaboration), Performance of a silicon pixel vertex detector in the SLD, in C. H. Albright, P. H. Kasper, R. Raja, and J. Yoh (eds.), *The Fermilab Meeting: DPF92,* Singapore: World Scientific, 1993, pp. 1758–1760; C. J. S. Damerell, CCD vertex detectors in particle physics, *Nucl. Instrum. Methods A,* **342**, 78–82, 1994.
51. For a recent summary see G. Hall, Radiation damage to silicon detectors, *Nucl. Instrum. Methods A,* **368**: 199–204, 1995, and references therein.

52. K. M. Smith, GaAs detector performance and radiation hardness, *Nucl. Instrum. Methods A,* **368**: 220–223, 1995.

53. F. Borchelt et al., First measurements with a diamond microstrip detector, *Nucl. Instrum. Methods A,* **354**: 318–327, 1995.

54. D. Christian et al., The development of two ASIC's for a fast silicon strip detector readout system, *IEEE Trans. Nucl. Sci.,* **NS-36**: 507–511, 1989; T. Zimmerman, A high speed, low noise ASIC preamplifier for silicon strip detectors, *ibid.,* **NS-37**: 439–443, 1990.

55. J. Antos et al., The SVX II silicon vertex detector upgrade at CDF, *Nucl. Instrum. Methods A,* **360**: 118–124, 1995; M. Tanaka et al., LSI design and data-acquisition architecture for a silicon microvertex detector at the KEK B-factory, *ibid.,* **342**: 149–155, 1994; W. J. Haynes, Silicon tracker data acquisition, in G. J. Blanar and R. L. Sumner (eds.), *Proc. 6th Int. Conf. Electron. Particle Phys.,* Chestnut Ridge, New York: LeCroy Res. Syst., 1997, pp. 25–42.

56. R. Wigmans, High resolution hadronic calorimetry, *Nucl. Instrum. Methods A,* **265**: 273–290, 1988.

57. R. J. Yarema et al., A high speed, wide dynamic range digitizer circuit for photomultiplier tubes, *Nucl. Instrum. Methods A,* **360**: 150–152, 1995; T. Zimmerman and M. Sarraj, A second generation charge integrator and encoder ASIC, *IEEE Trans. Nucl. Sci.,* **NS-43**: 1683–1688, 1996.

58. E. D. Bloom and C. Peck, Physics with the crystal ball detector, *Annu. Rev. Nucl. Part. Sci.,* **33**: 143–197, 1983.

59. M. A. Akrawy et al., Development studies for the OPAL end cap electromagnetic calorimeter using vacuum photo triode instrumented leadglass, *Nucl. Instrum. Methods A,* **290**: 76–94, 1990.

60. For more on the search for matter-antimatter asymmetry see D. M. Kaplan, Fixed-target *CP*-violation experiments at Fermilab, in A. K. Gougas et al. (eds.), *1st Int. Four Seas Conf.,* CERN Yellow Report 97-06, Geneva, Switzerland: CERN, 1997, pp. 25–33, and references therein.

61. D. M. Kaplan et al., The HyperCP data acquisition system, in G. J. Blanar and R. L. Sumner (eds.), *Proc. 6th Int. Conf. Electron. Particle Physics,* Chestnut Ridge, New York: LeCroy Res. Syst., 1997, pp. 165–177.

62. CDF Collaboration, F. Abe et al., The CDF detector: An overview, *Nucl. Instrum. Methods A,* **271**: 387–403, 1988.

Reading List

Good introductory treatments of special relativity and particle physics may be found in textbooks on modern physics, for example:

A. Beiser, *Concepts of Modern Physics,* 5th ed., New York: McGraw-Hill, 1995.

K. S. Krane, *Modern Physics,* 2nd ed., New York: Wiley, 1995.

H. C. Ohanian, *Modern Physics,* 2nd ed., Englewood Cliffs, NJ: Prentice-Hall, 1995.

There are also more elementary and abbreviated treatments in general-physics textbooks, for example:

D. Halliday, R. Resnick, and J. Walker, *Fundamentals of Physics (Extended),* 5th ed., New York: Wiley, 1997.

H. C. Ohanian, *Physics,* Vol. 2, 2nd ed., New York: Norton, 1989, Expanded.

Introductory texts on particle physics include

D. J. Griffiths, *Introduction to Elementary Particles,* New York: Harper and Row, 1987.

D. H. Perkins, *Introduction to High Energy Physics,* 3rd ed., Menlo Park, CA: Addison-Wesley, 1987.

Detailed treatments of particle detection techniques may be found in

R. M. Barnett et al. (Particle Data Group), *Review of Particle Physics, Phys. Rev. D,* **54**: 1–720, 1996.

T. Ferbel (ed.), *Experimental Techniques in High Energy Nuclear and Particle Physics,* 2nd ed., Singapore: World Scientific, 1991.

W. R. Leo, *Techniques for Nuclear and Particle Physics Experiments,* 2nd ed., New York: Springer, 1994.

DANIEL M. KAPLAN
Illinois Institute of Technology

KENNETH S. NELSON
University of Virginia